Science Bulletin 64 (2019) 814–822

Contents lists available at ScienceDirect

Science Bulletin

journal homepage: www.elsevier.com/locate/scib

Science Bulletin
www.scibull.com

Article

Dynamically reconfigurable topological edge state in phase change photonic crystals

Tun Cao [a,*], Linhan Fang [a], Ying Cao [a], Nan Li [b], Zhiyou Fan [b], Zhiguo Tao [b]

[a] School of Optoelectronic Engineering and Instrumentation Science, Dalian University of Technology, Dalian 116024, China
[b] China North Vehicle Research Institute, Beijing 100072, China

ARTICLE INFO

Article history:
Received 28 December 2018
Received in revised form 3 February 2019
Accepted 12 February 2019
Available online 23 February 2019

Keywords:
Phase change materials
Photonic crystals
Topological edge states
Tunability
Reconfigurability

ABSTRACT

The observation of topological edge states (TESs) revolutionized our understanding of scattering and propagation of electromagnetic (EM) waves. Supported by topological robustness, the TES at the interface between trivial and non-trivial insulators was not reflected from the structural disorders and imperfections. Recently topological photonic crystals (PhCs) were demonstrated to obtain remarkable one-way propagation of the TES, having the advantages of lossless propagation, dense integration, and high fabrication tolerance over conventional PhCs. Nevertheless, the lack of reversible switching of TES possesses significant limitations in helicity/spin filtering and tunable photonic devices. We proposed a topological PhC based on a prototypical phase-change material, $Ge_2Sb_2Te_5$ (GST225) to solve the problem. We find that at a particular frequency, the TES within the structure can be reversibly switched between "on" and "off" by transiting the GST225 structural state between amorphous and crystalline. Moreover, the topology of the PhC was maintained since the tuning of TES was achieved by varying the refractive index of GST225 instead of the structural geometry. This provides a continuous change of the spectral position of the photonic bandgap and TES by gradually crystallising the GST225. We show that the phase change of GST225 from amorphous to crystalline and vice versa can be engineered in nanoseconds. Our proof of concept may offer a platform for dynamically tuning the TESs that might otherwise be challenging to attain in photonic systems. We expect it to have potential applications for photonic devices in topological optical circuits and scatter-free one-way light propagation.

1. Introduction

The discovery of the topological states of electron topological insulators [1–3] aroused the search for analogous states in artificial micro/nanostructures supporting electromagnetic (EM) waves [4–7]. Owing to the topological protection, the photonic edge modes at the interface between the synthetic structures with different topology (trivial and non-trivial) are a lack of backscattering. Such topological edge states (TESs) can robustly transmit the EM energy against structural imperfections and disordered areas that do not vary the topology of the system, which provides possibilities for topological photonic devices [8,9]. Previous methods in topological order for photons were realized in synthetic photonic structures under an external magnetic field [10–12], where the magnetic field was used to break time reversal (TR) symmetry [13]. However, it is inconvenient to employ strong magnets at GHz frequencies, and materials with intense magnetic response are absent at the higher frequency region (i.e., visible-infrared spectrum). These hamper the further understanding and manipulation essential for realistic applications. To this end, the photonic structures where TR symmetry was either broken by dynamically modifying the system's parameters [14] or preserved [15] have proven promising. Engineering synthetic gauge fields [16,17], or spatial [18,19] or temporal modulation [20] mimicking the effective magnetic field were shown to be feasible alternatives to a real magnetic field, which can generate the desired topological features. Although the photonic TES was successfully realized in a system with TR symmetry [21,22], active control of the TES in synthetic optical media was rarely explored. Recently, a photonic topological insulator (PTI) with mechanical reconfigurability was demonstrated in the GHz region [4,6], where they tuned the TES by adjusting the geometric parameters of PTI that slows the tuning speed of the TES; very few of dynamically reconfigurable PTI were undertaken. Very recently, switching of the TES by both liquid crystal orientation and temperature were reported [23,24]; moreover, researchers experimentally demonstrated the nonlinearity-engineered topological transition in electric circuits [25] and electromagnetic resonators array [26], which paves the way for active controlling of the TES. However,

SPECIAL TOPIC: Electromagnetic Metasurfaces: from Concept to Applications.

* Corresponding author.
E-mail address: caotun1806@dlut.edu.cn (T. Cao).

https://doi.org/10.1016/j.scib.2019.02.017
2095-9273/

most of the techniques discussed above are limited by the switching speed of TESs. The possibility of ultrafast control of TESs via a reconfigurable synthetic gauge field can lead to various applications in the areas of helicity/spin filters, tunable electronic and analogous optical devices [27,28]. This leads us to search for an efficient and straightforward method that can efficiently engineer the TESs, for example by forming the PTI using an active medium.

In the research of phase change materials, Ge–Sb–Te (GST) alloys were pioneered by Ovshinsky [29]. GSTs have a remarkable portfolio of properties. The GST phase can be reversibly and rapidly changed between amorphous and crystalline phases, and the electronic and optical properties of the two phases differ radically. This feature qualifies GST as prominent candidates to substitute rewritable, non-volatile data storage, i.e. FLASH, owing to their high cyclability, fast switching speed, outstanding scalability and thermal stability [30,31]. To improve the electrical and physical performance of GST in nanoelectronics, synthetic GST nanostructures have recently drawn considerable attention [32]. Recently, GST continues to be a key ingredient for non-volatile, tunable nanophotonic devices due to a significant contrast of the permittivity observed between the two structural states [33,34]. It is because a tremendous change of permittivity can shift the structure's resonance, which in turn causes altered functionalities. Note that, lately fabrication techniques of the GST-based nanostructures have been well developed, and a few exciting functionalities of the nanostructures were realized, i.e., tunable chiral metamaterials based on stacked nanopillars in paired enantiomer shapes with a GST layer in between [35], all-dielectric switchable metamaterials based on the GST [36], and subwavelength resonators for the surface phonon-polaritons confinement [33]. Among a variety of GST alloys, $Ge_2Sb_2Te_5$ (GST225) has dominated the field and been extensively employed as a recording medium in optical storage formats.

In this work, a 100 nm thick GST225 film residing on a Si substrate was fabricated and experimentally characterized. The variable angle spectroscopic ellipsometry (VASE) measured data reveals that the GST225 refractive index can change drastically by transforming its state from amorphous to crystalline. Based on the above measurement, we continue to demonstrate, both analytically and numerically, a two-dimensional (2D) photonic crystal (PhC) made of a GST225 pillars array. In the proposed PhC, the photonic TESs are derived by deforming cylinders with a honeycomb lattice into cylinder hexagons with a triangular lattice. Unlike the previously reported topological PhCs, we facilitate a dynamically reconfigurable TES by reversibly changing the phase of the GST225 pillars. Our thermal-electric model illustrates that short 51 and 5 ns phase transition times can be attained via 18 and 41 V biasing voltages (V_b) for both crystallisation and re-amorphisation accordingly, enabling fast switching between the on/off TES modes. Our strategy will be profitable for a class of topological photonic devices where in situ control of the TES is a major concern.

2. Materials and methods

2.1. Sample fabrication

The 100 nm thick GST225 film was deposited on substrate by a radio frequency (RF) sputtering system (AJA Orion 5), where the substrate is a 2 μm thick un-doped double side polished Si (0 0 1) wafer with resistivity > 2×10^4 Ω cm. Previous to the deposition, the Si substrate was cleaned ultrasonically in acetone, isopropanol, and deionized water and lastly dried with dry nitrogen. Afterward, the GST225 film was sputter-deposited on the Si substrate with a deposition rate of 1 Å/s and RF power of 30 W. The 99.99% pure GST225 sputtering target has a diameter of 50.8 mm and the target-sample distance is 140 mm. The complex refractive index of the GST225 film is experimentally obtained by the variable angle spectroscopic ellipsometry (VASE) for both amorphous and crystalline states. We use a Tauc-Lorentz model for the fitting.

2.2. Theoretical model

In this work, a commercial software, COMSOL Multiphysics, based on the finite element method was used to construct the numerical model. In the model, the dispersive complex refractive index of GST was obtained from Fig. 1. The PhC has 23 unit cells in the x-axis with 8 unit cells of both trivial and non-trivial (topological) regions along the y-axis. The structure is surrounded by the scattering boundary. The system was excited with a spin-down (right-propagating) dipole point source $S_- = H_0 e^{i\omega t}(\hat{x} + i\hat{y})$, where H_0 is the amplitude, ω a frequency, $\hat{x}$ and $\hat{y}$ the unit vectors along x- and y-directions respectively. This generates an in-plane magnetic field with right circularly polarization (RCP) thus the out-of-plane E_z field with wave function of negative angular momentum. The point source located around the interface between trivial and nontrivial parts of the PhC, which well matched the profile of the mode propagating along + x direction. The photonic band dispersion is calculated using a Wave Optics module from COMSOL Multiphysics.

3. Results and discussion

3.1. The measurement of optical properties of GST225

The 100 nm thick GST225 film was deposited on a substrate by a radio frequency (RF) sputtering system (AJA Orion 5), where the substrate is a 2 μm thick un-doped double-side polished Si (0 0 1) wafer with >2×10^4 Ω cm resistivity. Prior to the deposition, the Si substrate was cleaned ultrasonically in acetone, isopropanol and deionized water and lastly dried with dry nitrogen. Afterwards, the GST225 film was sputter-deposited on the Si substrate with a 1 Å/s deposition rate and 30 W RF power. The 99.99% pure GST225 sputtering target had a 50.8 mm diameter and the

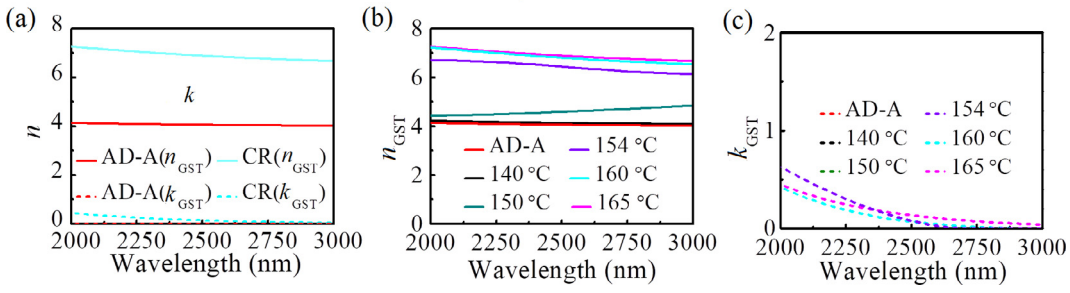

Fig. 1. The complex refractive index of GST225 film. (a) The complex refractive index ($n = n_{GST} + i \times k_{GST}$) of the GST225 film with structural states of as-deposited amorphous (denoted as AD-A) and crystalline (denoted as CR). n was measured by the VASE across a spectral range of 2,000–3,000 nm. The VASE measured (b) n_{GST} and (c) k_{GST} of the GST225 film at various temperatures. The thickness of the GST225 film is 100 nm.

target-sample distance was 140 mm. The complex refractive index of the planar GST film (over the spectral range of 2,000–3,000 nm) is displayed in Fig. 1a. The complex refractive index was experimentally obtained by VASE for both amorphous and crystalline states. We used a Tauc-Lorentz model for fitting. By thermally crystallising the as-deposited amorphous (AD-A) GST225 layer, the real part of its refractive index (n_{GST}, solid lines) had a significant contrast and was weakly dispersive, whilst the imaginary part (k_{GST}, dotted lines) was small over the spectral region. The radical variation in the n_{GST} between the structural states can shift the photonic bandgap (PBG), that in turn reversibly switched the TES "on/off" at a fixed frequency. The variation of refractive index ($n = n_{GST} + i \times k_{GST}$) of GST225 was caused by a bonding change from predominantly covalent in the amorphous phase to resonant bonds in the crystalline phase [31]. Moreover, in the mid-infrared (M-IR) spectral region, the photon energy is smaller than the optical band gap of both amorphous and crystalline GST225. This leads to a negligible extinction coefficient, k_{GST} in the spectral range from 2,500 to 3,000 nm. We crystallised the as-deposited amorphous GST225 film by heating it for 30 min at 165 °C on a hot plate in a flowing argon atmosphere. However by employing optical or electrical pulses techniques, one can reliably switch the GST in nanosecond [33,34]. Note, the GST225 film is gradually crystallised. This creates the intermediate phases that have regions of both amorphous and crystalline states [37]. By controlling the annealing process (i.e., annealing time and temperature), the intermediate phase and the crystallization fraction of GST225 can be modified correspondingly. This can lead to a gradual change of the GST225 refractive index. Such an appealing feature can result in a continuously tunable photonic device. To illustrate the continuous tuning of TES in the proposed PhC, the complex refractive index of the GST225 film at various heating temperatures was experimentally measured, as seen in Fig. 1b and c. By increasing the temperature from room temperature to 165 °C, we found that n_{GST} increased with temperature (Fig. 1b) while maintaining k_{GST} around zero (Fig. 1c) in 2,500–3,000 nm. The gradual change of the real part controls the continuous shift of the spectral positions of PBG and TES, and the negligibly small imaginary part contributes to small losses in TES transmission. As is observed in Fig. 1b, there is a noticeable change of n_{GST} when the temperature changes from 150 to 154 , indicating that the 100 nm thick GST225 film is mostly crystallized at $T \geq 154$. The optical properties of the amorphous and crystalline phases differ vastly. Another significant advantage of the GST225 intermediate phases is their non-volatile storage property; the intermediate phases were stable at room temperature, and thermal energy was only needed for the switching process, not for sustaining a particular phase. This apparently makes the continuously tunable photonic topological insulator interesting from a green technology perspective.

3.2. Design of topological photonic crystals based on GST225 rods

In condensed matter, topologically nontrivial states can transmit spin currents or charges along the interface; however, these transfers are prohibited in the bulk. Topological photonic systems have an analogous feature regarding the one-way [11,38] and spin-polarized photonic propagation. Even if the photon transport in the bulk is prevented by a bandgap induced through the synthetic gauge or magnetic fields, it can occur along the boundaries in the form of edge states. These edge states appear between topologically different structures where the spin-Chern number varies across the interface. This can be obtained either at an interface between trivial and topologically nontrivial structures, or the interface that separates two topological domains with various or opposite topological indices. This work will focus on the first type of topological interface. A PhC is a periodic photonic nanostructure that controls photons' motions in much the same way that ionic lattices control electrons' motions in solids [39]. Our proposed scheme is a topological protecting PhC built of a GST225 pillars array. As sketched in Fig. 2a, the structure consists of two parts: non-trivial and trivial topologies. Both the top and bottom Au layer are used to load the biasing voltage (V_b) on the GST225 pillars array. As the electric current passed through the GST225 pillars array, the Joule heat can transit the phase of the GST225 pillar and hence, modulate its refractive index. The crystallisation and melt-quenched amorphisation of each GST225 pillar were achieved by the currents through the $V_b = 18$ and 41 V, accordingly. Fig. 2b shows that each part is formed by a triangular lattice made of six pillars per unit cell. The pitch of the pillars array is $L_0 = 900$ nm, where the diameter and height of the GST225 rods are $d = 180$

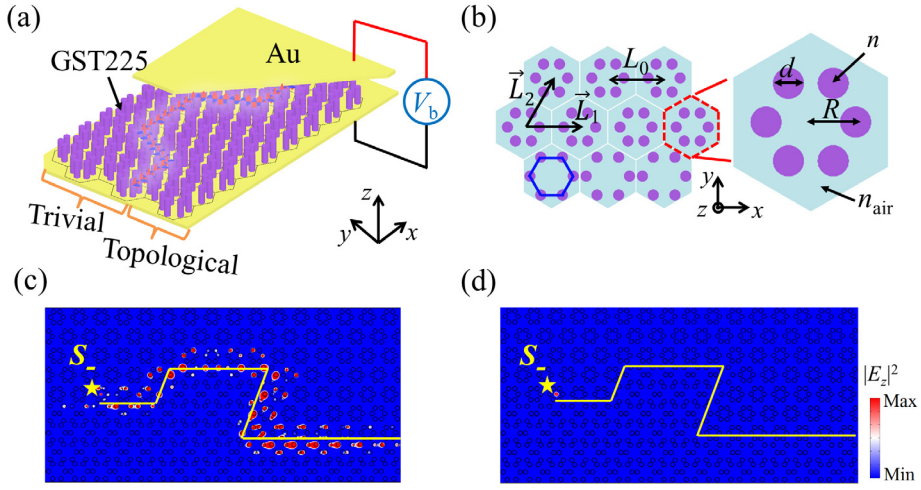

Fig. 2. The GST225 pillars based topological 2D PhC and its functionality of switching "on/off" the light propagation. (a) The sketch of the topological 2D PhC made of GST225 pillars. The structural state of GST225 can be switched by applying an external electrode. (b) Left panel: a schematic view of the synthetic cells consisting of six GST225 rods. The unit cells of the topological PhC are triangular lattices (marked by the red dashed line). The blue solid line labels the artificial hexagon cell. $\vec{L}_1$ and $\vec{L}_2$ are unit vectors with a length of L_0, the lattice constant. Right panel: zoom-in picture of the hexagon cell, where R is the length of the hexagon edge and d the diameter of the pillar. The n and n_{air} are refractive indexes of GST225 rods and air surrounding environment, accordingly. Switching "on/off" the light propagation along the rhombus-shaped path (an interface between the trivial and non-trivial regions indicated by a yellow line) at $\lambda = 2{,}174$ nm via the state transition between the (c) amorphous and (d) crystalline, where (c) and (d) share an identical colour bar.

and h = 100 nm, respectively. Relying on the hopping energy associated with the space between the pillars, the PhC can feature a trivial or non-trivial band-structure topology. At the interface between the two parts with the different topologies, the TES appears owing to the optical analog of quantum spin Hall effect of electrons. The reconfigurable speed of the TES in a PhC depends on the speed of refractive index change of its constitutive dielectric. Therefore, for real-time in-situ device switching, the eventual aim is to search for the dielectric with a rapid variation of refractive index. Based on this idea, GST225 pillars are chosen to create the PhC. As was discussed for Fig. 1, the tuning of GST225 refractive index can be experimentally realised by external heating. We considered incident light with a transverse magnetic (TM) polarisation across a wide M-IR region, where a vast change of n_{GST} was experimentally observed through the phase change between amorphous and crystalline, as shown in Fig. 1a; for example, $n_{a-GST} \approx 4 + 0.05i$, $n_{c-GST} \approx 7 + 0.2i$ from 2 to 3 μm. n_{a-GST} and n_{c-GST} represent the refractive index of the GST225 for both as-deposited amorphous and crystalline states, respectively.

Fig. 2c and d numerically illustrate the intensity distributions of the E_z field ($|E_z|^2$) in the topological PhC with various structural states of GST225 at λ = 2,174 nm. For amorphous GST225 (Fig. 2c), it presents that TM polarized light can be efficiently guided along a rhombus-shaped path at λ = 2,174 nm, indicating the excitation of TES at the ribbon edges within the bulk bandgap (see the discussion for Fig. 3d). By switching the state from amorphous to crystalline while maintaining λ = 2,174 nm, the propagation of the wave can be completely turned off (Fig. 2d). This is because the phase change (dielectric constant change) of the GST225 pillars does not vary the topological properties of the structure but alters the position of the PBG. This results in a bulk state at λ = 2,174 nm that cannot transmit the light along the interface (see the discussion in the Supplementary Section 4). Such a PhC can thus perform as a dynamically reconfigurable topological photonic device with a switchable TES. As is seen in Fig. 1c, at λ = 2,174 nm the k_{GST} of GST225 films for both amorphous and crystalline (T = 165 °C) states are 0.01 and 0.3 respectively. For the topological PhC made of amorphous GST225 pillars (k_{GST} = 0.01), a penetration depth of 17.3 μm at λ = 2,174 nm can be obtained [40]. This enables its length to be about 0.07 times the effective penetration depth, indicating that the signal at the output is reduced by a factor of 1.07. Thus, a low reduction of the signal at the output is achieved. By crystallizing the topological PhC, the k_{GST} is significantly increased to 0.3 with a penetration depth of 600 nm that reduces the output signal by a factor of 7.89.

The ribbon-shaped 2D topological PhC was simulated by solving Maxwell equations using a commercial finite element method (FEM) package, COMSOL Multiphysics. The PhC has 23 unit cells in the x-axis with 8 unit cells of both trivial and non-trivial (topological) regions along the y-axis. The structure is surrounded by the scattering boundary. The system was excited with a spin-down (right-propagating) dipole point source $S_- = H_0 e^{i\omega t}(\hat{x} + i\hat{y})$, where H_0 is the amplitude, ω a frequency, and $\hat{x}$ and $\hat{y}$ the unit vectors along x and y directions respectively. This generates an in-plane magnetic field with right circular polarization (RCP), thus the out-of-plane E_z field with a wave function of negative angular momentum. The point source located around the interface between trivial and nontrivial parts of the PhC, which well matched the profile of the mode propagating along the + x direction. The position of the point source was marked by the star symbol in Fig. 2c and d. Because the harmonic source preserves TR symmetry followed by the Maxwell equations, our structure exhibits helical topological edge states. When the system was injected by a point source S_-, light propagation along the rightward unidirection was observed (see Fig. 2c), as anticipated from the bulk topology. Our proposed structure has a rather simple geometry that can be experimentally realized if a successful deposition of thin GST225 film was obtained.

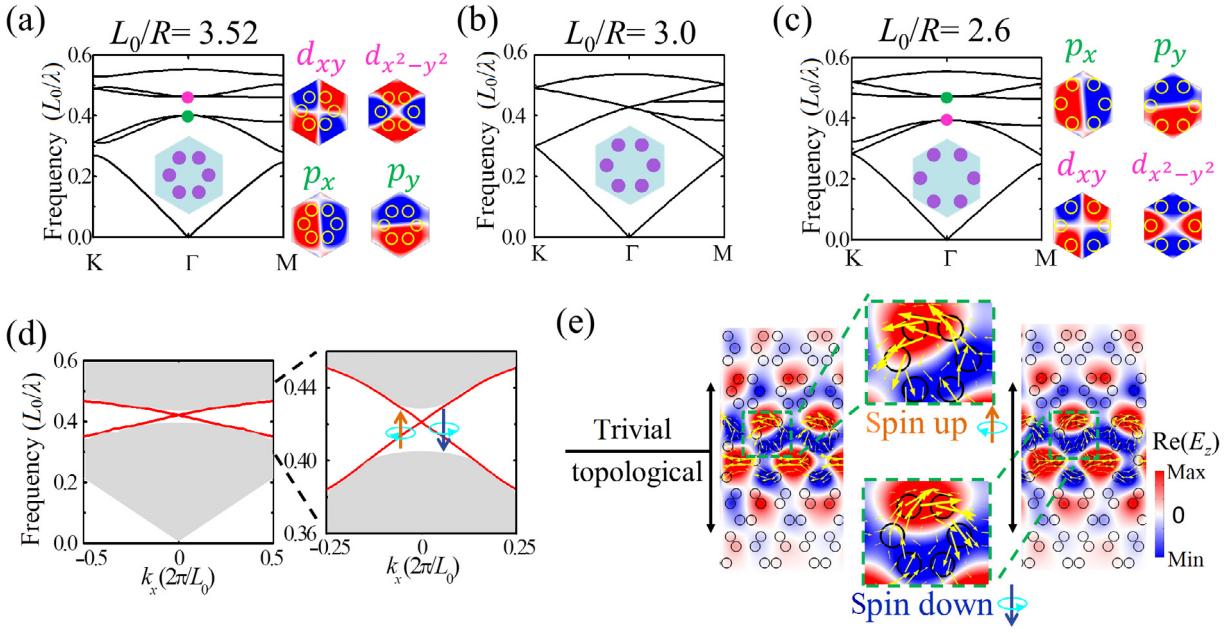

Fig. 3. The photonic bandgraph of the topological 2D PhC made of GST225 pillars. Left column: dispersion relations of TM mode for the 2D PhCs composed by the amorphous GST225 cylinders for (a) L_0/R = 3.52, (b) L_0/R = 3.0, (c) L_0/R = 2.6. The insets present the unit cells for each case. The hole radius and lattice constant were fixed at r = 90 nm and L_0 = 900 nm. Right column: the distributions of Re(E_z) of p_x and d_{xy} photonic orbitals supported by the artificial atom around the Γ point for (a) L_0/R = 3.52 and L_0/R = 3.0, (c) L_0/R = 2.6. The dashed rectangles covering a unit lattice point in (a)–(c) were used to envisage the two and four-fold nature of the $p_x(p_y)$ and $d_{xy}(d_{x^2-y^2})$ mode symmetries. Particularly, the Re(E_z) field distributions at the bottom band edge ($p_x(p_y)$, green) and the upper ($d_{xy}(d_{x^2-y^2})$, pink) for the compressed trivial PhC were inverted relative to the expanded non-trivial PhC that possessed Re(E_z) field distributions at the lower ($d_{xy}(d_{x^2-y^2})$, pink) and upper ($p_x(p_y)$, green) band edge around the Γ point. (d) Dispersion relations of TM mode for the ribbon-shaped 2D topological PhC composed by the amorphous GST225 cylinders. (e) The field distributions of Re(E_z) at $k_x = \pm 0.05(2\pi/L_0)$ in the ribbon-shaped 2D topological PhC.

Given by the experimental realisation of our proposed methodology, a 3D model is built up to investigate the light confinement in the out of the plane, where the height of the GST225 pillar (h_{rod}) needs to be taken into account. The two horizontal Au plates are not only the electrodes but also forbid the photonic bands with nonzero k_z to drop into topological band gap [41]. Damping of light waves in the Au plates is considered by employing a complex dielectric constant for Au. We determine h_{rod} = 100 nm that is identical to the thickness of the GST225 film shown in Fig. 1. The 3D simulation is performed to show that the waves can be confined along z-axis well between the two Au cladding layers (see Figs. S1, S2 online).

In this work, we focus on the spectral range of 2,000–3,000 nm, one of the atmospheric transmission windows, which allows the photonic device to work with negligible disturbance from water vapor dust, and other atmospheric influences [42]. The low phonon energies of GST will enable them to be transparent in the spectra of 2,000–3,000 nm [43]. The fast transition between two structural phases of the GST, allows it to be ideal for the switchable photonic devices [44].

3.3. Reconfigurable photonic band

In order to further explore the origin of the reconfigurable TES, we now calculate the photonic band dispersion in the topological PhC for the different states of GST225. We first investigate the propagation of the EM wave excited by a harmonic source via the TESs in a finite topological PhC. The Maxwell equations are expressed as [39],

$$\frac{\partial H}{\partial t} = -\frac{1}{\mu_0}(\nabla \times E + S_H),\ \frac{\partial E}{\partial t} = \frac{1}{\varepsilon(r)}(\nabla \times H - S_E), \tag{1}$$

where the harmonic TM modes are considered with magnetic field $H = (H_x, H_y, 0)$ and electric field $E = (0, 0, E_z)$, μ_0 the magnetic permeability in free space, $\varepsilon(r)$ the position-dependent permittivity, S_H (S_E) the external magnetic (electric) current density produced by the sources. The TESs can be excited by not only a linearly polarized harmonic source ($E = E_0 e^{i\omega t}\hat{z}$) but also circularly polarized sources $S_- = H_0 e^{i\omega t}(\hat{x} + i\hat{y})$ and $S_+ = H_0 e^{i\omega t}(\hat{x} - i\hat{y})$ launching light characterized by E_z fields with wave functions of negative and positive angular momenta, respectively. Herein, we focus on the circularly polarized source. The light wave transmitting through the topological PhC for a particular harmonic mode of frequency ω can be described by [39],

$$\left[\frac{1}{\varepsilon(r)}\nabla \times \nabla \times\right] E_z(r)\hat{z} = \frac{\omega^2}{c^2} E_z(r)\hat{z}, \tag{2}$$

where c is the speed of light in vacuum and Eq. (2) is derived from the Eq. (1). The magnetic field is obtained by the Faraday relation $H = [i/(\mu_0\omega)]\nabla \times E$. In our proposed structure, the Bloch theorem is employed for the present system as $\varepsilon(r)$ is periodic, shown in Fig. 2b.

For a small separation between the two Au plates, the field distribution inside the PhC is uniform along the z-axis [24]. Such a 3D system can be well approximated using 2D z-invariant simulation [5,22,24]. Herein in order to simplify the model, we consider the structure to be infinite along the z-direction, which reduces the problem to two dimensions. A pair of decoupled pseudospin states was expressed by [5]

$$p_\pm = (p_x \pm i p_y)/\sqrt{2}, \tag{3}$$

$$d_\pm = (d_{x^2-y^2} \pm i d_{xy})/\sqrt{2}, \tag{4}$$

where p_x (p_y) and d_{xy} ($d_{x^2-y^2}$) represent the orbitals carried by the artificial atoms for the E_z field at the Γ point and have identical symmetry to those of the electronic orbitals of the atoms in general solids. The positive (p_+, d_+) and negative (p_-, d_-) angular momenta of the wave function of the E_z field correspond to the up and down pseudospins and propagate in opposite directions in the proposed PhC. This leads to an optical equivalent to the quantum spin Hall effect of electrons.

In this work, we formed a ribbon-shaped topological PhC by distorting a honeycomb lattice of GST225 pillars, while maintaining the artificial hexagonal crystal composed of six neighbouring rods and C_6 symmetry. This crystal symmetry plays a key role in pseudo-TR symmetry that offers a Kramers doubling in the same manner as TR symmetry in an electronics system [45]. A PBG can be induced by compressing or expanding the hexagon (decreasing or increasing the R) in each primitive cell in the six-atom basis. Fig. 3 shows the dispersion relations of TM mode for the 2D PhCs with L_0/R of 3.52, 3.0 and 2.6, as well as for a ribbon-shaped topological PhC, where the initial state of the GST225 cylinder was amorphous and its complex refractive index was extracted from the measured data in Fig. 1a, R is the length of hexagon edge and L_0 the lattice constant. In the left column of Fig. 3a, we see that by shrinking the unit cell to L_0/R = 3.52, a topologically trivial PhC was obtained, in which a PBG was opened between the reduced normalized frequencies (L_0/λ) of 0.402 and 0.462 with a gap of 0.06.

Herein a double degeneracy in the band diagram emerges around the Γ point, which can be recognized as p_x (p_y) and d_{xy} ($d_{x^2-y^2}$) modes that are consistent with the consideration of symmetry. The d_{xy} ($d_{x^2-y^2}$) and p_x (p_y) orbitals correspond to even and odd spatial parities, respectively [5]. At the bottom of the highest band, the distribution of the real part of the E_z field (Re(E_z)) showed a p_x (p_y) mode symmetry; however, at the top of the lowest band, the mode symmetry was d_{xy} ($d_{x^2-y^2}$) (right column of Fig. 3a). As was observed within the dashed rectangles circling a honeycomb lattice site, the p_x (p_y) mode exhibited two lobes in each side about the y- (x-) axis, mimicking the two-lobed atomic orbitals. Likewise, the d_{xy} ($d_{x^2-y^2}$) mode was characterised by four lobes with one in each quadrant, analogous to the atomic d_{xy} ($d_{x^2-y^2}$) orbitals. The p bands are below the d bands, for which the Chern numbers are zero indicating that the photonic crystals (PhC) have a trivial state [5]. At L_0/R = 3, the p_x (p_y) and d_{xy} ($d_{x^2-y^2}$) modes turn degenerate around the Γ point, and double Dirac cones occur (Fig. 3b). This is because the PhC with L_0/R = 3 is equal to the honeycomb lattice of individual rods, which enables the doubly degenerate Dirac cones to be nothing but those around the K and K' point in the Brillouin zone of honeycomb lattice composed by a rhombic primitive cell of two sites [46]. At L_0/R = 2.6, a global PBG was once again opened near the Dirac point (the left column of Fig. 3c). The gap was between the reduced normalised frequencies (L_0/λ) of 0.393 and 0.472, leading to a gap of 0.08 that is slightly wider than the topologically trivial structure shown in Fig. 3a. However, now the field distributions of Re(E_z) around the Γ point have a reversal. For example, the lower and upper frequency sides of the PBG have d_{xy} ($d_{x^2-y^2}$) and p_x (p_y) symmetry modes accordingly (right column of Fig. 3c). This indicates a band inversion, which gives rise to a topologically non-trivial PhC.

The quantum spin Hall edge states possess a property of "spin filtered", where the down spin moves towards one direction, and the up spin propagates towards the other. These edge states are so-called "helical", similar with the correlation between momentum and spin of particle known as helicity [47,48]. Using Fig. 3d, we will then explain the helicity dependent one-way propagation along the rhombus-shaped interface between the non-trivial and trivial PhCs, as shown in Fig. 2c. The hole radius and lattice constant were fixed at r = 90 nm and L_0 = 900 nm for both topologically non-trivial (L_0/R = 2.6) and trivial (L_0/R = 3.52) sides of the

ribbon-shaped topological PhC. Both sides individually exhibit the C_6 symmetry; however, the C_6 symmetry was broken at the interface between the two sides. This broken symmetry lifts the degeneracy between the spin modes and permits the interaction of the modes, which can open a tiny gap at the Γ point. There were two distinct states (represented by the double degenerate red curves) within the gap between the two frequencies linking the lower and upper bands, which possess scatter-free propagation. As was observed in the central column of Fig. 3e, for the wave vector of $k_x = -0.05(2\pi/L_0)$, the Poynting vectors ($\vec{S}$) have a steady state electromagnetic (EM) energy flow in the downward direction, which corresponds to the pseudospin-up (↑) edge mode (marked by an orange up arrow). On the contrary, for $k_x = +0.05(2\pi/L_0)$ we observed a non-zero upward EM power flow relating to the pseudospin-down (↓) edge mode (marked by a blue down arrow). This clearly indicates counter propagations of EM energy at the sample edge relating to the two pseudospin states, the characteristic of a quantum spin Hall effect state [47–49]. As was discussed in Fig. 2c, these edge states enabled unidirectional propagation along the interface with sharp turns. Nevertheless, the presence of the edge state was not the only condition to obtain the scatter-free propagation. The other essential requirement was the lack of any bulk state at the same frequency in which the topologically protected propagation was desired. This can avoid the possible edge states from leaking into free space. In the right column of Fig. 3e, we illustrated the field distributions of Re(E_z) at the two typical momenta of $k_x = \pm 0.05(2\pi/L_0)$. We found that the two in-gap states located at the ribbon edges exponentially decayed into the bulk. We calculated the Chern numbers for pseudo spin-up and-down channels of $C_\pm = \pm 1$ by integrating Berry curvatures around the first Brillouzin zone respectively (see Section 2 and Fig. S3 online). Therefore, our proposed PhC is non-trivial topology.

In Fig. S4 (online), further simulations were performed to study the band diagrams of the TM mode for the crystalline PhC with $L_0/R = 3.52$ (Fig. S4a online), 3.0 (Fig. S4b online), 2.6 (Fig. S4c online), and the ribbon-shaped PhC (Fig. S4d online). As is observed in Figs. S4d–e (online), a pair of pseudo-spin-up and pseudo-spin-down edge states existed in the bandgap dividing the bulk bands of the ribbon-shaped 2D topological PhC. This proves that the structural state (refractive index) change of the constitutive GST225 cylinders does not vary the topological properties of the PhC. However, the location and size of the bandgap can be modulated by varying the state of the GST225. For the amorphous ribbon-shaped PhC (Fig. 3d), the bandgap covers the normalized frequency (L_0/λ) range from 0.394 to 0.461. By transiting the state from amorphous to crystalline, the bandgap was reduced and red-shifted such that it extended from 0.254 to 0.305 (Fig. S4d online). Note that for the TR symmetry that is not broken explicitly by the magnetic field (that is, the analogs of Z_2 topology), the topological protection against backscattering is only limited, becoming restricted to the defects that do not couple the two Kramers partners. This will reduce the robustness of TES against the disordered atoms at the rhombus-shaped (sharp bent) interface that does not induce such coupling. Namely, the light cannot maintain the unidirectional propagation along the rhombus-shaped interface if we introduce the deformed cylinders at the interface (see Fig. S5 online).

In Fig. 4a, thermal-electric model was carried out to study the temporal change of the GST225 pillar temperature under $V_b = 18$ and 41 V, which can switch "on" and "off" the light propagation along the rhombus-shaped interface at a fixed wavelength of $\lambda = 2{,}174$ nm. This modeling approach is developed by finite element method (FEM) solver within COMSOL. The structure built in the thermal-electric model is identical to that presented in Fig. 2a. The two fundamental state transitions of crystallisation and re-amorphisation occur on the various temperatures and time scales. Note, the whole system was in hydrogen (H_2) surroundings that can quickly dissipate the heat due to its much higher thermal conductivity compared to air. It is because one needs to quickly cool off the GST225 film to fully re-amorphise it. Herein, we focus on reversibly switching on/off the TES via an electrically driven state transition. The material thermoelectric properties for GST225 and Au employed in the model are summarized in Table 1. The GST225 pillar must be heated to a temperature above the crystallization temperature of $T_C = 433$ K but below the melting temperature of $T_M = 873$ K for the crystallization. Fig. 4a illustrates that the temperature in the amorphous GST225 pillar increased

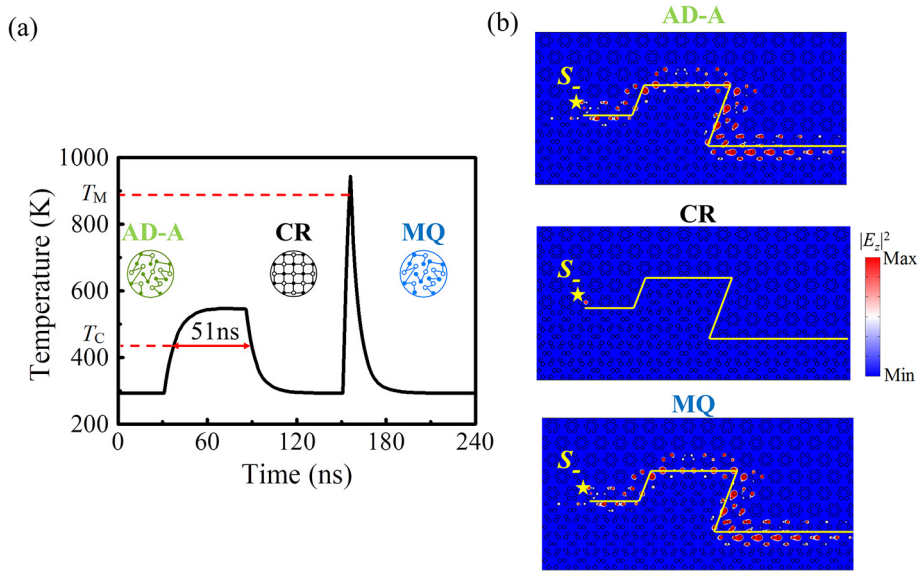

Fig. 4. The time-dependent temperature distributions of the GST225 pillar in the topological 2D PhC. 3D-FEM simulation of (a) time-dependent temperature distributions of the GST225 pillar. The as-deposited amorphous (AD-A) GST225 pillar was electrically heated beyond $T_C = 433$ K to change to crystalline (CR) GST225 under $V_b = 18$ V. For re-amorphisation, the CR-GST225 was annealed above $T_M = 873$ K. This temperature was attained by employing $V_b = 41$ V. Subsequent quenching produces the melt-quenched (MQ) state GST225. (b) The field distributions of Re (E_z) at $\lambda = 2{,}174$ nm in the ribbon-shaped 2D topological PhC when the state of GST225 pillar is AM (top panel), CR (central panel), and MQ (bottom panel) respectively.

Table 1
Material thermal properties used in the Heat transfer model.

	Special heat capacity CS (J/kg K)	Density ρ (kg/m^3)	Thermal conductivity k (W/(m k))	Electrical conductivity σ (S/m)	Relative permittivity ε_r	Seebeck coefficient S (V/K)
Au	129 [50]	19,300 [50]	20 Thickness 10 nm [50]	Temperature dependence [51]	6.9 [52]	Temperature dependence [53]
$Ge_2Sb_2Te_5$	220 [54]	6150 [55]	Temperature dependence [55]	Temperature dependence [56]	Temperature dependence [57]	Temperature dependence [58]

with the time for which the TES was excited at V_b = 18 V. This results in a rapid increase of the GST225 pillar temperature, which goes above T_C = 433 K after 7 ns to start changing the GST225 phase from amorphous to crystalline, where the GST225 can be partially crystallized and form in-between states having areas of both amorphous and crystalline states [38]. 7 ns was the time difference between t = 30 and 37 ns, where the temperature of the GST225 pillar was 293 and 446 K, respectively. We then completely crystallise the GST225 pillar by constantly heating it with V_b = 18 V, which provides thermal energy to maintain the temperature above T_C but below T_M for ~51 ns [34]. A complete crystallisation of the GST225 pillar can entirely switch off the light propagation along the rhombus-shaped interface. The GST225 pillar temperature starts dropping down to 293 K (room temperature) when the V_b = 18 V was off, owing to thermal energy dissipation into the H_2 surroundings.

To reversibly switch on the TES, the crystalline GST225 pillar needs to be re-amorphised. A backward re-amorphisation (from

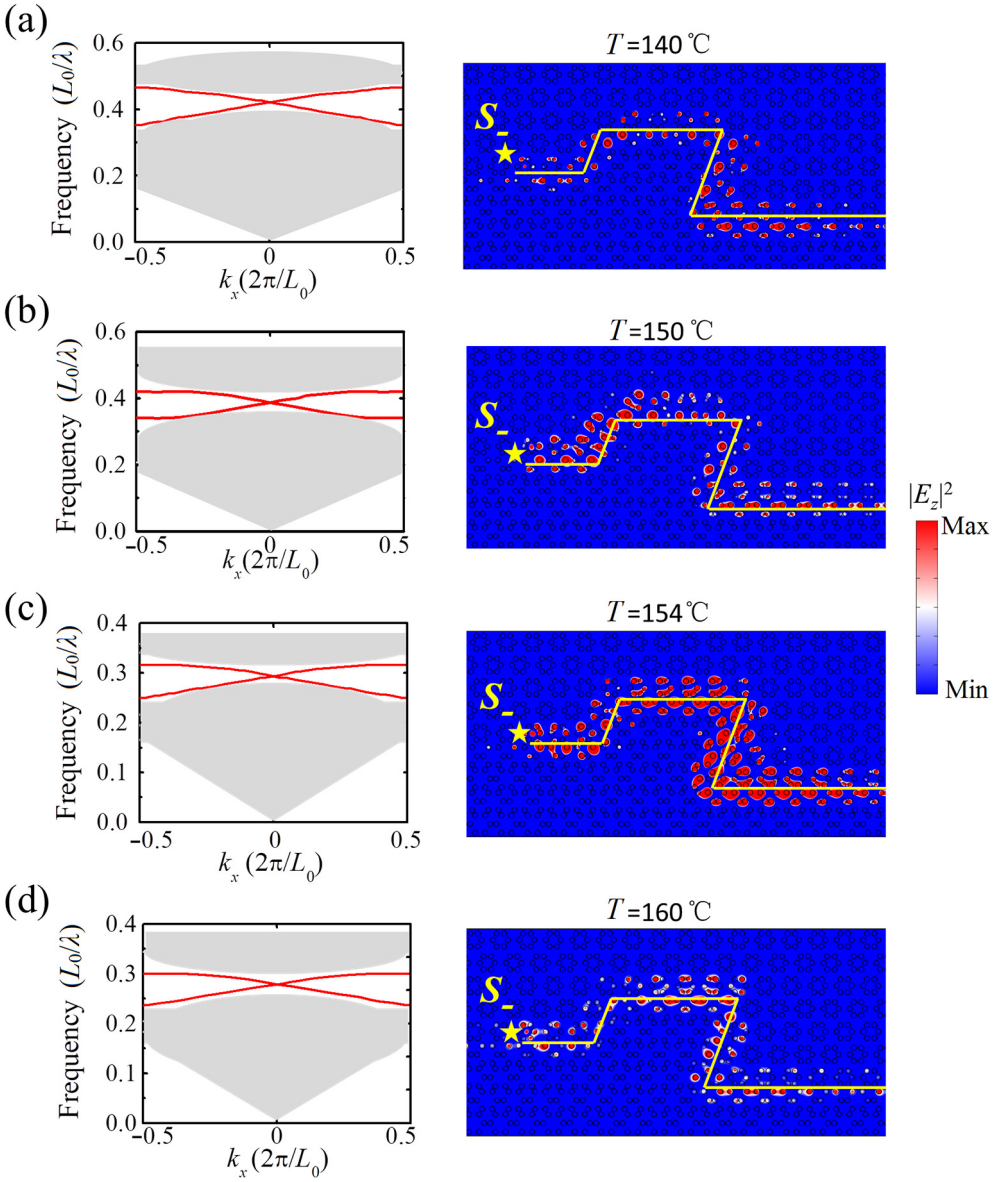

Fig. 5. The bandgap and light propagation in ribbon-shaped PhC at various temperatures. The bandgap of the ribbon-shaped PhC (left column) and light propagating along the interface with a rhombus-shaped defect (right column) for (a) λ = 2,174 nm with T = 140 °C, (b) λ = 2,222 nm with T = 150 °C, (c) λ = 3,092 nm with T = 154 °C, and (d) λ = 3,333 nm with T = 160 °C.

the crystalline to amorphous) can be induced by boosting the local temperature rapidly above the T_M through a melt-quenching procedure. Note, the crystal lattice of GST225 requires time to relax from the amorphous to crystalline state, resulting in the longer duration of the phase change than the time required to melt-quench the lattice into the amorphous state. It was shown that a repetitive excitation can recrystallize the GST225 film [59]. In this work, V_b = 41 V with a biasing time of 5 ns enables the reversible phase change from the crystalline to amorphous. During the re-amorphisation procedure, the V_b = 41 V can provide high thermal energy to increase the temperature rapidly above the T_M and melt the GST225. By switching off the V_b = 41 V, the subsequent fast cooling can quench the melt into the amorphous state that avoids any recrystallization of the atomic structure. One can again turn off the TES by setting the V_b to 18 V.

This can explain the reconfigurability of the TES, e.g. the light propagation along the rhombus-shaped interface was reversibly switched between "on" and "off" at the fixed λ = 2,174 nm by altering the state of GST225 cylinder between amorphous and crystalline as shown in Fig. 4b. When the GST225 was amorphous, the edge state of λ = 2,174 nm (L_0/λ = 0.414) was located inside the bandgap of the ribbon-shaped PhC (Fig. 3d). Thereby, the light propagated along the rhombus-shaped interface without scattering to the bulk (top and bottom panels of Fig. 4b). For the crystalline ribbon-shaped PhC, the edge state redshifted to λ = 3,333 nm (L_0/λ = 0.270) due to the variation of bandgap caused by the GST225 phase transition (Fig. S4d online). Therefore, the light at λ = 2,174 nm no longer propagated along the rhombus-shaped interface (central panel of Fig. 4b). It was shown that the structural stability of the GST225 nanorods can remain stable during its reversible phase transition [60], indicating the possible experimental implementation of our proposed structure. In Table S1 (online), we calculated the electric current and consumed electric power acting on the topological PhC in the thermal-electric model.

The TES can be continuously modulated by controlling the temperature that determines the crystallization portion. Fig. 5(a–d) illustrates the bandgap of the ribbon-shaped PhC (left column) and light propagating along the interface with a rhombus-shaped defect (right column) at λ = 2,174, 2,222, 3,092, and 3,333 nm for the temperatures (T) of 140, 150, 154, and 160 °C, where the λ located at the ribbon edges within the bulk bandgap as changing the temperature (crystallisation portion). In the model, the complex refractive index of the GST225 at different temperatures is obtained from the experimental data (Fig. 1b and c). It is obvious that varying the temperature permits direct control over the frequency location of the PBG and TES, which can drastically modulate the transmission properties of the system.

In order to check robustness of the TESs to non-homogeneous temperature distribution, we consider the topological photonic crystal composed of three sections that are under the different temperatures (see Fig. S6 online). It shows that the excited TES at λ = 2,174 nm can still transmit through the various temperature regions unidirectionally, implying that the TES remains stable against these moderate changes of the temperature.

4. Conclusion

To conclude, we propose a concept of robust control of TES in a dynamically reconfigurable topological PhC made of GST225 rod arrays. The topological feature in the PhC was allowed by optically resembling the spin-Hall effect. This leads to TESs at the interface between the non-trivial and trivial parts of the crystal, where the light can propagate along arbitrarily shaped paths to a certain point without a back-reflection. We experimentally deposited and characterized the GST225 chalcogenide laminate, which shows a large refractive index contrast over the M-IR region by switching the state of GST225 between amorphous and crystalline. We theoretically derive the reconfigurability of the TES by constructing the 2D PhC using a deformed honeycomb lattice of GST225 pillars. The thermal-electric model shows that the GST225 phase can be reversibly changed in ~ 150 ns via biasing voltage, which causes an ultrafast variation in the GST225 refractive index, thus shifting the spectral location of TES. This reconfigurable platform enables the investigation of a variety of instrumental physical phenomena i.e. tunable spin switching and filtering. For example, we demonstrate that the PhC can fast switch on/off the propagation of TES at λ = 2,174 nm, which proves the versatility of the proposed reconfigurable platform for fulfilling unique device functionalities. These findings would be crucial in the development of the design possibilities of modern optical communication devices based on the spin-orbital angular momentum of light, spin-dependent transport and robust flow of light.

Conflict of interest

The authors declare that they have no conflict of interest.

Acknowledgments

This work was supported by International Science & Technology Cooperation Program of China (2015DFG12630) and Program for Liaoning Excellent Talents in University (LJQ2015021). The authors would like to acknowledge the ACTAlab led by Prof. Robert E Simpson from Singapore University of Technology and Design for providing the facility necessary for conducting the research.

Author contributions

T.C. conceived the idea of using phase change photonic crystals for obtaining reconfigurable topological edge state. T.C. designed the photonic crystals and performed numerical analysis. L.H.F., Y. C., N.L., Z.Y.F., and Z.G.T. carried out the simulations and prepared the figures. T.C. supervised the research. T.C. wrote the manuscript.

Appendix A. Supplementary data

Supplementary data to this article can be found online at https://doi.org/10.1016/j.scib.2019.02.017.

References

[1] Cao G, Liu H, Chen X-Q, et al. A simple and efficient criterion for ready screening of potential topological insulators. Sci Bull 2017;62:1649–53.
[2] Bernevig BA, Hughes TL, Zhang S-C. Quantum spin hall effect and topological phase transition in hgte quantum wells. Science 2006;314:1757–61.
[3] Zhang Y, Wang C, Liu G, et al. Temperature-induced Lifshitz transition in topological insulator candidate $HfTe_5$. Sci Bull 2017;62:950–6.
[4] Cheng X, Jouvaud C, Ni X, et al. Robust reconfigurable electromagnetic pathways within a photonic topological insulator. Nat Mater 2016;15:542–8.
[5] Wu L-H, Hu X. Scheme for achieving a topological photonic crystal by using dielectric material. Phys Rev Lett 2015;114:223901.
[6] Goryachev M, Tobar ME. Reconfigurable microwave photonic topological insulator. Phys Rev Appl 2016;6:064006.
[7] Furusaki A. Weyl points and dirac lines protected by multiple screw rotations. Sci Bull 2017;62:788–94.
[8] Lu L, Joannopoulos JD, Soljacic M. Topological states in photonic systems. Nat Phys 2016;12:626–9.
[9] Rodríguez-Lara BM, El-Ganainy R, Guerrero J. Symmetry in optics and photonics: A group theory approach. Sci Bull 2018;63:244–51.
[10] Wang Z, Chong Y, Joannopoulos JD, et al. Observation of unidirectional backscattering-immune topological electromagnetic states. Nature 2009;461:772–5.
[11] Poo Y, R-x Wu, Lin Z, et al. Experimental realization of self-guiding unidirectional electromagnetic edge states. Phys Rev Lett 2011;106:093903.

[12] Zhang C, Lu H-Z, Shen S-Q, et al. Towards the manipulation of topological states of matter: a perspective from electron transport. Sci Bull 2018;63:580–94.
[13] Lu Y-K, Peng P, Cao Q-T, et al. Spontaneous *T*-symmetry breaking and exceptional points in cavity quantum electrodynamics systems. Sci Bull 2018;63:1096–100.
[14] Estep NA, Sounas DL, Soric J, et al. Magnetic-free non-reciprocity and isolation based on parametrically modulated coupled-resonator loops. Nat Phys 2014;10:923–7.
[15] Lu L, Fu L, Joannopoulos JD, et al. Weyl points and line nodes in gyroid photonic crystals. Nat Photonics 2013;7:294–9.
[16] Hafezi M, Demler EA, Lukin MD, et al. Robust optical delay lines with topological protection. Nat Phys 2011;7:907–12.
[17] Wu Y-L. Unified field theory of basic forces and elementary particles with gravitational origin of gauge symmetry in hyper-spacetime. Sci Bull 2017;62:1109–13.
[18] Rechtsman MC, Zeuner JM, Plotnik Y, et al. Photonic Floquet topological insulators. Nature 2013;496:196–200.
[19] Xin Y, Huang Y, Lin K, et al. Self-template synthesis of double-layered porous nanotubes with spatially separated photoredox surfaces for efficient photocatalytic hydrogen production. Sci Bull 2018;63:601–8.
[20] Fang K, Yu Z, Fan S. Realizing effective magnetic field for photons by controlling the phase of dynamic modulation. Nat Photonics 2012;6:782–7.
[21] Mittal S, Fan J, Faez S, et al. Topologically robust transport of photons in a synthetic gauge field. Phys Rev Lett 2014;113:087403.
[22] Khanikaev AB, Shvets G. Two-dimensional topological photonics. Nat Photonics 2017;11:763–73.
[23] Li C, Hu X, Gao W, et al. Thermo-optical tunable ultracompact chip-integrated 1D photonic topological insulator. Adv Opt Mater 2018;6:701071.
[24] Shalaev MI, Desnavi S, Walasik W, et al. Reconfigurable topological photonic crystal. New J Phys 2018;20:023040.
[25] Hadad Y, Soric JC, Khanikaev AB, et al. Self-induced topological protection in nonlinear circuit arrays. Nat Electron 2018(1):178–82.
[26] Dobrykh DA, Yulin AV, Slobozhanyuk AP, et al. Nonlinear control of electromagnetic topological edge states. Phys Rev Lett 2018;121:163901.
[27] Liu J, Hsieh TH, Wei P, et al. Spin-filtered edge states with an electrically tunable gap in a two-dimensional topological crystalline insulator. Nat Mater 2014;13:178–83.
[28] Xiao Y-F, Gong Q. Optical microcavity: From fundamental physics to functional photonics devices. Sci Bull 2016;61:185–6.
[29] Ovshinsky SR. Reversible electrical switching phenomena in disordered structures. Phys Rev Lett 1968;21:1450–3.
[30] Wuttig M, Yamada N. Phase-change materials for rewriteable data storage. Nat Mater 2007;6:824–32.
[31] Shportko K, Kremers S, Woda M, et al. Resonant bonding in crystalline phase-change materials. Nat Mater 2008;7:653–8.
[32] Lieber CM, Wang ZL. Functional nanowires. MRS Bull 2007;32:99–108.
[33] Li P, Yang X, Mass TWW, et al. Reversible optical switching of highly confined phonon-polaritons with an ultrathin phase-change material. Nat Mater 2016;15:870–5.
[34] Wuttig M, Bhaskaran H, Taubner T. Phase-change materials for non-volatile photonic applications. Nat Photonics 2017;11:465–76.
[35] Yin X, Schaeferling M, Michel A-KU, et al. Active chiral plasmonics. Nano Lett 2015;15:4255–60.
[36] Wang Q, Rogers ETF, Gholipour B, et al. Optically reconfigurable metasurfaces and photonic devices based on phase change materials. Nat Photonics 2016;10:60–5.
[37] Lee B-S, Burr GW, Shelby RM, et al. Observation of the role of subcritical nuclei in crystallization of a glassy solid. Science 2009;326:980–4.
[38] Peng X, Sun M-X. Pollen tube, a one-way special train for special passengers. Sci Bull 2017;62:1165–6.
[39] Joannopoulos JD, Johnson SG, Winn JN, et al. Photonic crystals molding the flow of light. 2nd ed. Princeton: Princeton Univ; 2008.
[40] Phillips R. The feynman lectures on physics. Nature 2013;504:30–1.
[41] Li Y, Kita S, Munoz P, et al. On-chip zero-index metamaterials. Nat Photonics 2015;9:738–43.
[42] Tittl A, Michel A-KU, Schaeferling M, et al. A switchable mid-infrared plasmonic perfect absorber with multispectral thermal imaging capability. Adv Mater 2015;27:4597–603.
[43] Feng X, Mairaj AK, Hewak DW, et al. Nonsilica glasses for holey fibers. J Lightwave Technol 2005;23:2046.
[44] Michel AKU, Zalden P, Chigrin DN, et al. Reversible optical switching of infrared antenna resonances with ultrathin phase-change layers using femtosecond laser pulses. ACS Photon 2014;1:833–9.
[45] Fu L. Topological crystalline insulators. Phys Rev Lett 2011;106:106802.
[46] Ochiai T. Photonic realization of the (2+1)-dimensional parity anomaly. Phys Rev B 2012;86:075152.
[47] Hasan MZ, Kane CL. Colloquium: topological insulators. Rev Mod Phys 2010;82:3045–67.
[48] Wu CJ, Bernevig BA, Zhang SC. Helical liquid and the edge of quantum spin Hall systems. Phys Rev Lett 2006;96:106401.
[49] Qi X-L, Zhang S-C. Topological insulators and superconductors. Rev Mod Phys 2011;83:1057.
[50] Chen G, Hui P. Thermal conductivities of evaporated gold films on silicon and glass. Appl Phys Lett 1999;74:2942–4.
[51] Hw M, LD R. Handbook of chemistry and physics. Boca Raton: CRC; 2010.
[52] Shklyarevskii IN, Pakhomov PL. Separation of contributions from free and coupled electrons into real and imaginary parts of dielectric-constant of gold. Opt Spektrosk 1973;34:163–6.
[53] Matula RA. Electrical resistivity of copper, gold, palladium, and silver. J Phys Chem Ref Data 1979;8:1147–298.
[54] Kuwahara M, Suzuki O, Yamakawa Y, et al. Measurement of the thermal conductivity of nanometer scale thin films by thermoreflectance phenomenon. Microelectron Eng 2007;84:1792–6.
[55] Lyeo H-K, Cahill DG, Lee B-S, et al. Thermal conductivity of phase-change material $Ge_2Sb_2Te_5$. Appl Phys Lett 2006;89:151904.
[56] Kim Y, Hwang U, Cho YJ, et al. Change in electrical resistance and thermal stability of Nitrogen incorporated $Ge_2Sb_2Te_5$ films. Appl Phys Lett 2007;90:021908.
[57] Kuwahara M, Suzuki O, Taketoshi N, et al. Measurements of temperature dependence of optical and thermal properties of optical disk materials. Jpn J Appl Phys 2006;45:1419–21.
[58] Kurinec SK, Iniewski K. Nanoscale semiconductor memories: technology and applications. Boca Raton: CRC; 2013.
[59] Cotton RL, Siegel J. Stimulated crystallization of melt-quenched $Ge_2Sb_2Te_5$ films employing femtosecond laser double pulses. J Appl Phys 2012;112:123520.
[60] Hong S-H, Lee H, Choi Y, et al. Fabrication of multi-level switching phase change nano-pillar device using InSe/GeSbTe stacked structure. Curr Appl Phys 2011;11:S16–20.

Tun Cao received his B.Sc. degree in 2002 at Dalian University of Technology and Ph.D. degree in 2007 at University of Bristol. Afterwards, he worked as post-doctoral researcher at City University of London. In 2010, he worked at Yonsei University as a research assistant professor. In 2011, he joined Dalian University of Technology as an associate professor and became a professor in 2016. His research interests include nonlinear optical properties, metamaterials and photonic crystals.